Analysis of strong scattering at the micro-scale

Kasper van Wijk
Physical Acoustics Laboratory, Department of Geophysics, Colorado School of Mines, Golden, Colorado 80401, USA

Dimitri Komatitsch
Seismological Laboratory, 1200 E. California Boulevard, Mail Code 252-21, Pasadena, California 91125, USA

John A. Scales
Physical Acoustics Laboratory, Department of Geophysics, Colorado School of Mines, Golden, Colorado 80401, USA

Jeroen Tromp
Seismological Laboratory, 1200 E. California Boulevard, Mail Code 252-21, Pasadena, California 91125, USA

(Received 23 August 2003; revised 17 December 2003; accepted 22 December 2003)

Exploiting the fine structure of strongly scattered waves could provide a wealth of new information in seismology, ultrasonics, acoustics, and other fields that study wave propagation in heterogeneous media. Therefore, noncontacting laser-based measurements of ultrasonic surface waves propagating in a strongly disordered medium are performed in which the ratio of the dominant surface wavelength to the size of a scatterer is large, and waves that propagate through many scatterers are recorded. This allows analysis of scattering-induced dispersion and attenuation, as well as the transition from ballistic to diffusive propagation. Despite the relatively small size of the scatterers, multiple scattering strikingly amplifies small perturbations, making changes even in a single scatterer visible in the later-arriving waveforms. To understand the complexity of the measured waveforms, elastic spectral-element numerical simulations are performed. The multiple-scattering sensitivity requires precise gridding of the actual model, but once this has been accomplished, we obtain good agreement between the measured and simulated waveforms. In fact, the simulations are invaluable in analyzing subtle effects in the data such as weak precursory body-wave diffractions. The flexibility of the spectral-element method in handling media with sharp boundaries makes it a powerful tool to study surface-wave propagation in the multiple-scattering regime. [DOI: 10.1121/1.1647480]

PACS numbers: 43.20.Gp, 43.20.Jr, 43.35.Cg, 43.35.Pt [YHB] Pages: 1006–1011

I. INTRODUCTION

Indications of multiple scattering in seismic waves have been observed,[1,2] but questions remain how to characterize media in which energy is multiply scattered (e.g., Ref. 3) Exciting advances have been made in using the later-arriving arrivals—or coda—of multiply scattered waves to detect minute changes in disordered media (e.g., Refs. 4–6), and the cross correlation of equipartitioned waves has been exploited to retrieve the Green's function between two detectors.[7–10]

In previous work we have described a tunable multiple scattering system, consisting of a block of aluminum with a disordered pattern of grooves cut in it.[11,12] Surface waves propagating parallel to the grooves are not scattered, but as we increase the angle between the scatterers and the direction of surface-wave propagation, scattering increases. Bulk properties of the propagation—including attenuation and dispersion—were studied to describe scattering on the *macroscopic* scale,[11] and we used a radiative transfer model to study the *mesoscopic* scale of the medium in terms of scattering and absorption mean-free paths.[13,13b] Here, we introduce two-dimensional (2D) numerical simulations of the physical system, based on the spectral-element method (SEM) (e.g., Ref. 14) to model this ultrasonic experiment with sharp topographic features, and investigate subtle details in the laboratory data on the scale of the individual scatterer, i.e., the *microscopic* scale.

Henceforth, we refer to the vertical component of the particle velocity measured in laboratory experiments as *data* and to the numerical results as *simulations*.

II. PHYSICAL EXPERIMENT

The setup of the experiment is shown in Fig. 1. A 200 V repetitive pulse is used to excite an angle-beam transducer mounted on the surface of an aluminum block of dimensions $x=232\ \text{mm}\times y=215\ \text{mm}\times z=280\ \text{mm}$. The transducer wedge has a footprint of $x=70\ \text{mm}\times y=42\ \text{mm}$. The angle of the transducer is such that its output in the aluminum block is mainly a broadband surface (Rayleigh) wave, effectively planar in the transverse (y) direction, with a dominant wavelength around 6 mm.

The wave field is detected along the x direction by a scanning laser vibrometer that measures absolute particle velocity on the surface of the sample via the Doppler shift (e.g.,

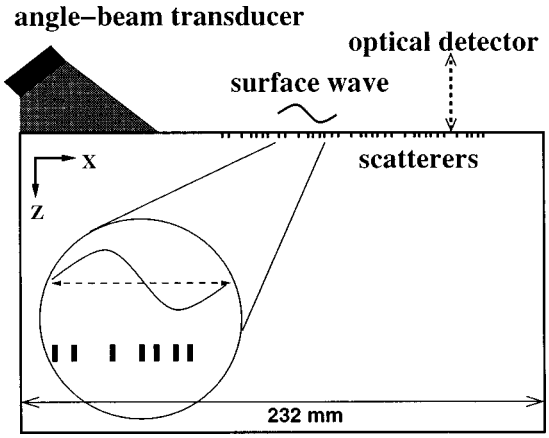

FIG. 1. Schematic setup of the experiment. The angle-beam transducer generates a Rayleigh wave that is multiply scattered by the grooves cut across one face of the aluminum block in the *y* direction. Vertical particle velocity is recorded by the laser Doppler vibrometer.

Refs. 11, 15). The signal is digitized at 14-bit resolution using a digital oscilloscope card, while the entire setup is positioned on a vibration isolation table to reduce background noise.

The aluminum block has a Fibonacci pattern of aligned linear grooves machined into one face. This sequence is quasiperiodic, but increases in complexity as it gets longer.[16] Theoretical and experimental results for transmission through Fibonacci multilayers have been published in Ref. 17. These authors show that minima in the transmission coefficient (as a function of wave number) become deeper as the number of layers in the Fibonacci multilayer increases, asymptotically leading to true band gaps. Analytic solutions for the Fibonacci scattering problem exist,[18] although they were not used in this article.

The grooves are nominally 1 mm wide (*x* direction), 2.75 mm deep (*z* direction), and 1 or 2 mm apart, but to represent the actual groove pattern more accurately in the numerical model, we scanned the surface at 2400 dots per inch (90 dots per mm), allowing us to include variations—coming from mechanical machining—in the average width of the grooves and the surface between grooves, which we call a nongroove.

III. NUMERICAL MODELING

The SEM is a high-order variational numerical technique[19,20] that combines the flexibility of the finite-element method with the accuracy of global pseudospectral techniques. Widely used in seismology,[14,21–23] here the SEM is used to simulate wave propagation at ultrasonic frequencies in a model that contains a large number of sharp grooves. The simulations can be compared to measurements at every surface location, because the optical detector can record at any location on the surface of the block (Fig. 1). The source in the simulations is the analytic solution to a Rayleigh wave,[24] and detectors are located in a line directly in front of the source. Intrinsic losses (i.e., anelastic effects) are so weak in aluminum[11] that attenuation is negligible.

The block is modeled by a mesh with cells whose size is on the order of a scatterer (i.e., a groove). The total number

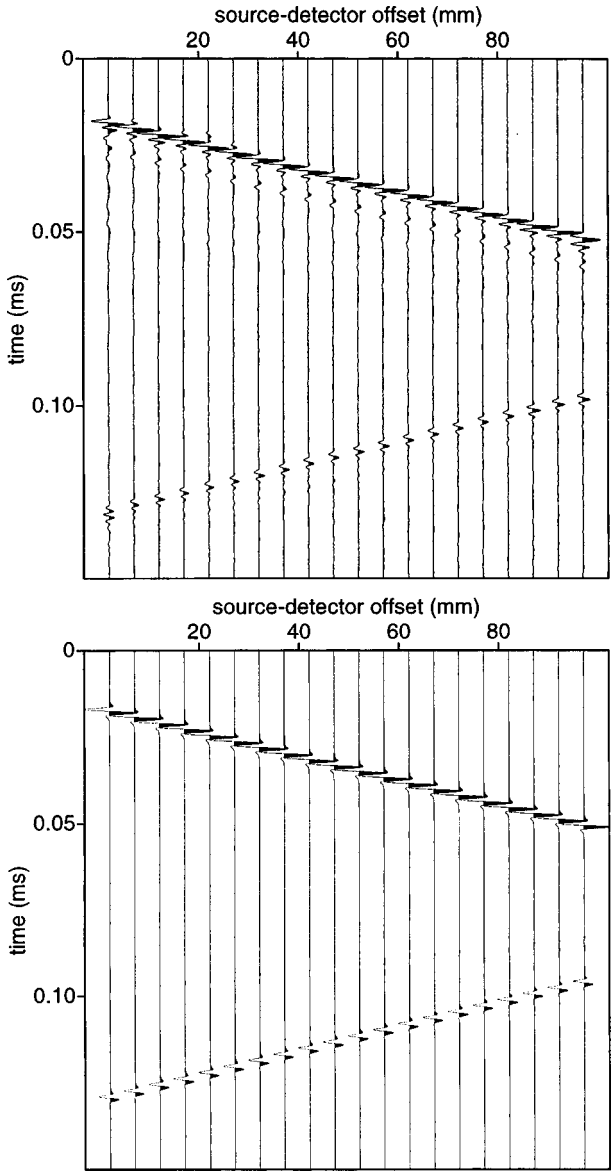

FIG. 2. Data (top) and simulations (bottom) for wave paths on the smooth side of the model.

of cells (spectral elements) is $232\,(x)\times 202\,(y)=46\,864$. In a classical finite-element method, the wave field is interpolated on these cell points. In the SEM, we use Lagrange polynomials of degree $N=4$ to interpolate the wave field in each quadrangular cell; the total number of grid points is 751 561. The time step Δt in the explicit integration scheme is 10 ns and we propagate the signal for 0.2 ms. Besides modeling the rapid topographic variations of the grooves, reflections off all boundaries of the block are included via free-surface boundary conditions, which are naturally taken into account by the SEM.

IV. COMPARING DATA AND SIMULATIONS

We compare data and simulations at 20 detector locations at 5-mm increments on the smooth face of the model, and on the first 42 nongrooves along a line perpendicular to the grooves (strong scattering). In both experiments, the source–detector distance (offset) for the first trace is 2 mm.

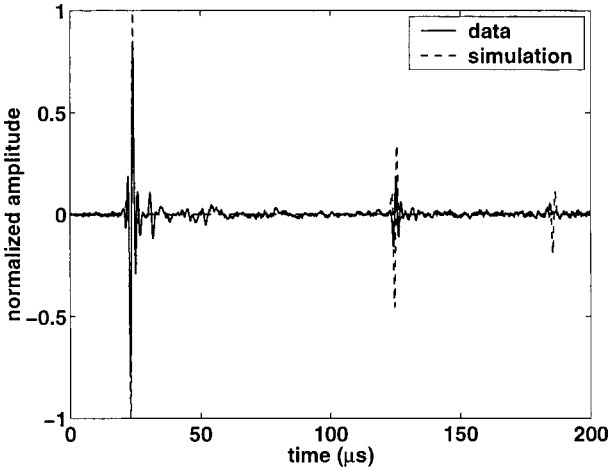

FIG. 3. Comparison between data and simulations for detector 1 on the smooth side of the model.

The data and simulations on the smooth aluminum surface are shown in Fig. 2. Both panels show a large direct surface-wave arrival, followed by a reflection from the far end of the aluminum block. The wavelet in the data has some energy after the main pulse caused by ringing in the transducer. This energy is not included in the source term of the simulations and will therefore limit our ability to fit the data. The data show little intrinsic losses and no evidence of reflections from the sides of the block, which means that the source energy emitted has little geometrical spreading, justifying 2D elastic simulations.

Also, we observe that the source wedge acts as an additional scatterer in the model, causing the maximum correlation on the smooth side of the aluminum to be smallest for detector 1. This near-field effect can be seen in the differences in amplitude and phase in the direct arrival and more clearly in the reflected event (Fig. 3), when compared to the other traces in Fig. 2. The second reflection from the edge of the block near the source is almost undetected in the data, because it requires the Rayleigh wave to travel along the surface between the bottom of the source wedge and the aluminum block. This is not an obstacle in the simulations, because the source is modeled by an analytically incident Rayleigh wave. This becomes even clearer from the simulated event at 190 μs. This is the surface wave that reflected once more from the side of the block near the source. The presence of the source wedge suppressed this event entirely in the laboratory measurements.

Figure 4 shows the data (top) and simulations (bottom) for waveforms in the strong scattering case. At each groove, energy is partially reflected, causing the direct arrival to be attenuated and the group velocity to be lowered compared to the unscattered wave propagation. The strongest events are interfering surface waves, which look qualitatively similar in the two panels. These strong events show coherence in the sense that a single phase can be tracked from one detector location to the next, whereas for late times, scattering causes arrivals to be incoherent from trace to trace.

Next, we compute the normalized cross correlation between simulations and data in 10-μs windows along the trace. If the wave fields are identical in the time window, a value of unity is assigned to the center of that window. Figure 5 contains the windowed, normalized cross correlation as a function of time, averaged over all source–detector distances. A correlation of unity is unlikely, because, for instance, the numerical simulations lack the random noise of the laboratory measurements, the ringing of the source, and the damping by the presence of the wedge observed in Fig. 3.

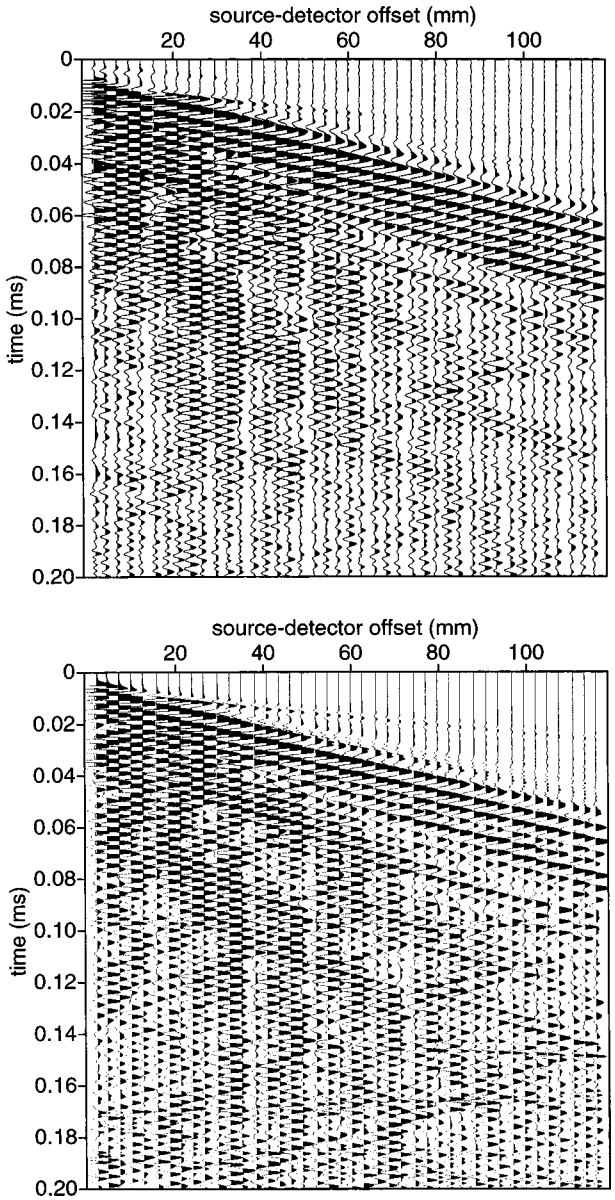

FIG. 4. Data (top) and simulations (bottom) for wave paths traveling perpendicular to the grooves (i.e., in the x direction). The main energy consists of surface waves bouncing between grooves, but the small-amplitude, faster events are body waves diffracted at the grooves.

The correlation between data and simulations on the smooth side of the model is visibly large for the direct wave and the reflection for all detectors. The average correlation for all 42 detectors on the grooved side first increases with time, as the coherent wave reaches the receivers at greater distance from the source. After the coherent energy has passed all receivers ($t > 0.1$ ms), the average correlation decreases. This shows that small discrepancies between the physical and numerical models on the order of a fraction of

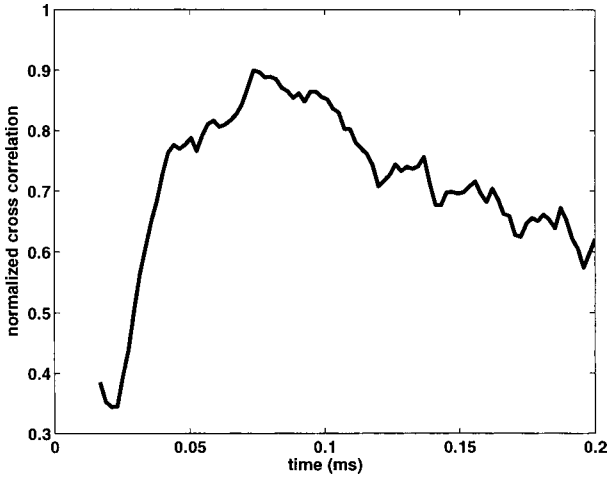

FIG. 5. Average normalized correlation between data and simulations for the 42 detectors as a function of time, on the grooved side of the model. Time windows of identical traces would have a correlation of 1.

the size of a single scatterer consistently decrease the accuracy of the simulations with time. The same effect is seen in coda wave interferometry[4] and diffusing wave spectroscopy;[5] these techniques derive their great sensitivity to small changes in a medium from the repeated sampling of the change by waves that bounce back and forth many times.

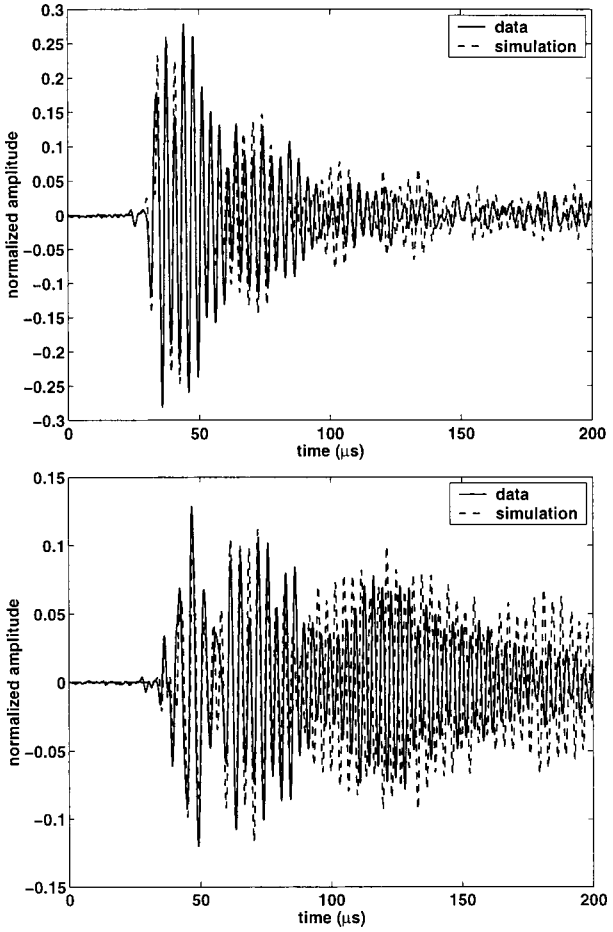

FIG. 6. Comparison between data and simulations on a thick (top) and a thin nongroove (bottom). Note the relatively stronger amplitudes at later times in the right panel.

In addition, both data and simulations on a nongroove with the size on the order of 1 mm show considerably more energy at later times than do traces on the thicker nongrooves. An example of this is detector 12, compared to detector 4 (Fig. 6): the relatively thin ridge of aluminum under detector 12 is excited in a 300-kHz resonance. While this mode is too low in frequency to represent multiple scattering of energy in the nongroove, it is possible that this resonance is a flexural mode of the thin nongrooves.[25] The power in the simulations of the thin nongrooves is visibly enhanced relative to the measurements (Fig. 7). We believe this is because the machined grooves are not perfectly rectangular, while the numerical mesh includes only fixed rectangular shapes whose dimensions are the average width and depth from the scan. In effect, imperfections in the machining reduce the Q of these resonances. This effect—plus the absence of the damping wedge in the simulations—results in the fact that the simulations have overall higher power than the measurements (Fig. 4).

V. DISCUSSION

In the strong-scattering case, relatively lower-amplitude and faster events arrive before the main surface-wave energy; Fig. 4 shows two coherent events with the *P*-wave velocity of aluminum. The first, starting at $t=0$, is caused by the angle-beam transducer producing some *P* waves in addition to surface-wave energy. This event is not present in the simulations, because the source is a pure Rayleigh wave. The second event with a *P*-wave velocity cannot be seen until the 6th or 7th trace at 0.01 ms, but is confirmed by the simulations.

To support the existence of these body-wave precursors to the surface-wave energy, we conducted a second experiment, in which the source is mounted on the face of the aluminum model with a single groove. In this case, the source is driven by a 5-cycle tone burst, centered around the resonant frequency of 500 kHz of the source transducer, as opposed to the broader-band signal used before. The particle velocity before and past a single groove is depicted in the top

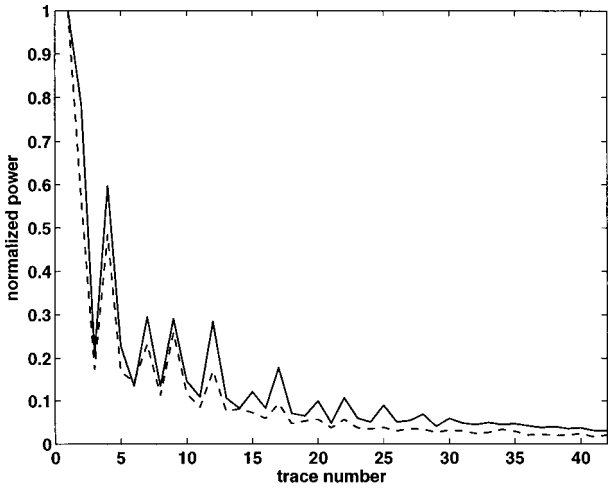

FIG. 7. Comparison between the normalized power in data and simulations. Especially for the detectors on thin non-grooves (detectors 4, 7, 9, 12, 15, 17, etc.), the simulations show more power.

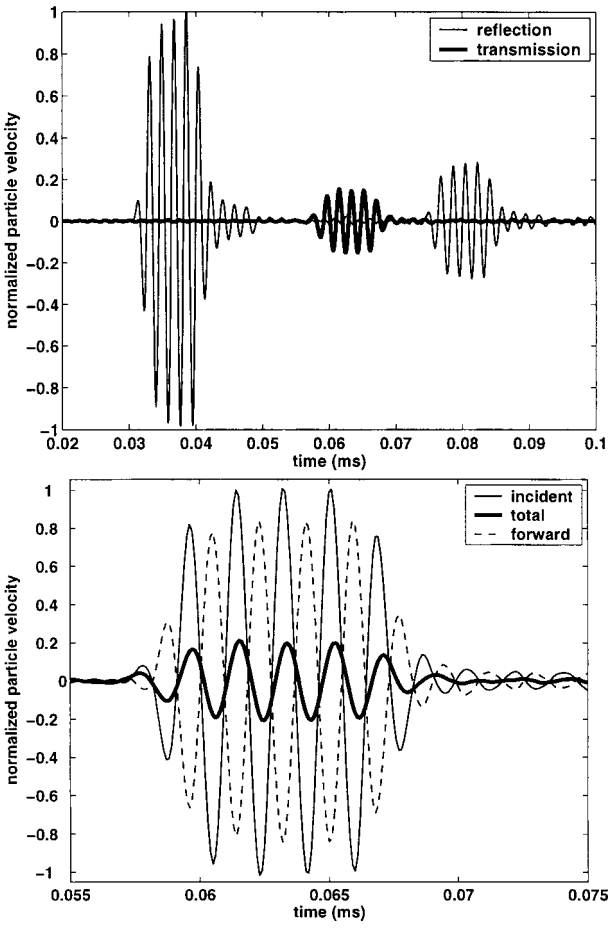

FIG. 8. Top: particle velocity measured before and after a single groove. The thinner line shows first the arrival of the incident field, followed by the backscattered signal from the groove. The thicker line is the total field past the scatterer, consisting of the incident plus the forward-scattered field. Bottom: decomposition of the total field (thick solid) past the groove into an incident (thin solid) and forward scattered component (dashed).

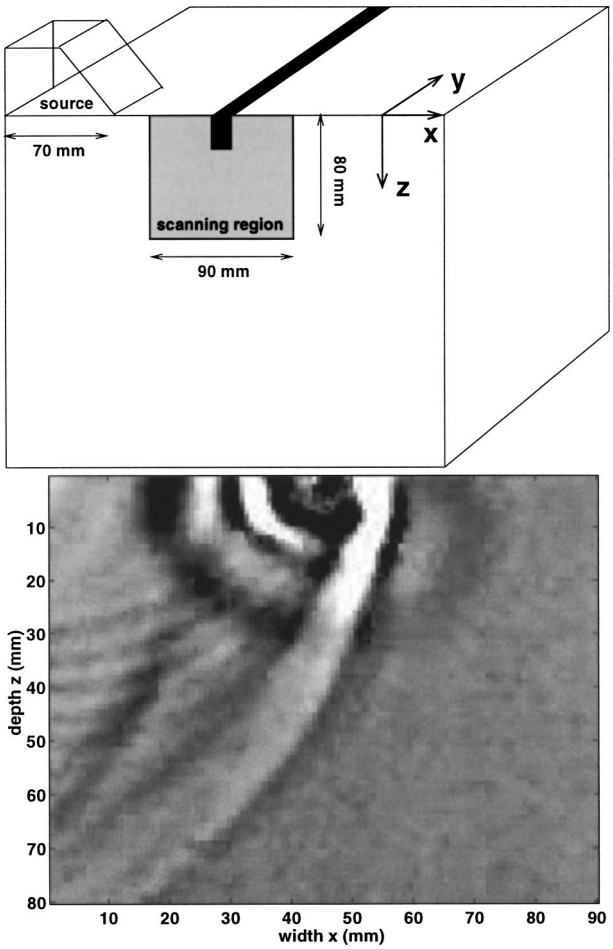

FIG. 9. Top: experimental configuration, where the source is perpendicular to a single groove on the top of the block, while the detector scans part of the (x,z) plane. Bottom: snapshot at $t=0.06$ ms of particle motion in the scanned region after the incident field scattered off a single groove. A movie of this experiment can be viewed at ⟨http://acoustics.mines.edu/onedee.html⟩.

panel of Fig. 8. The transmitted and reflected total intensity (the square of the particle velocity) is on the order of 0.04 and 0.06 times the incident field, respectively. This means that roughly 90 percent of the energy at this particular frequency is diffracted by a single scatterer. Lower frequencies are less influenced by the groove. This is why in the data with many grooves the dominant frequency after a few grooves drops from approximately 500 kHz to roughly 250 kHz.

The total transmitted field can be decomposed in the incident field and the forward-scattered field. By measuring the incident field at the same source–detector distance on the smooth side of the aluminum, we are able to estimate the forward-scattered field directly. Note that the forward-scattered field estimated in the bottom panel of Fig. 8 is 180 deg out of phase with the incident field, with a scattering strength of 0.8, making our scattering anisotropic. This strong out-of-phase forward scattering is known as the extinction paradox, observed in the shadow zone directly behind scatterers.[26]

The measurement is repeated with the detector scanning the side of the model (top panel of Fig. 9). The bottom panel of Fig. 9 shows a snapshot of particle motion, measured shortly after the incident wave interacted with the single groove. The side of the aluminum block breaks the symmetry of the Rayleigh-wave motion purely in the *x*- and *z* direction, creating particle motion in the *y* direction. Higher frequencies in the upper left part are due to ringing of the source, and the incident field is the strong event extending from top to bottom. The circular events are body waves scattered off the single groove. Scattering to body waves is stronger in the backward direction, but significant *P*-wave energy travels ahead of the surface wave, causing the precursors observed in Fig. 4. These spherical body-wave fronts diffracted at the individual grooves arrive before the Rayleigh waves and may be analogous to precursors to the seismic phase PKKP in global seismology[27] that some authors believe to be caused by scattering at the rough boundary between the Earth's outer core and mantle.[28,29]

VI. CONCLUSIONS

Laser ultrasonics provides a powerful tool for studying the fine structure of multiply scattered waves. Being able to place the detector, in effect, inside the scattering medium for surface waves allows one to directly visualize diffraction,

scattering, and mode conversion. However, the resulting waveforms in strong scattering media become increasingly complicated with time. Thus, it is useful to have the ability to make precise elastic simulations. In this study we have applied the numerical spectral-element method to simulate surface-wave multiple scattering in a grooved block of aluminum. Comparing the simulations to the data allowed us to analyze subtle imperfections in the physical model as well as precursory body-wave diffractions and flexural resonances of the grooves. The ability to handle complex boundaries with sharp edges makes the spectral-element method an ideal tool for laboratory ultrasonics.

ACKNOWLEDGMENTS

This work was supported by the Consortium Project on Seismic Inverse Methods for Complex Structures at the Center for Wave Phenomena, the National Science Foundation (EAR-0111804 and EAR-0003761), and the Army Research Office (DAAG55-98-1-0277 and DAAD19-03-1-0292). We thank Francisco José Sánchez-Sesma for the use of his Rayleigh wave code and Roel Snieder, Ken Larner, and Matt Haney for stimulating discussions. Finally, we are thankful for the many useful suggestions of the two anonymous reviewers. This is contribution No. 8928 of the Division of Geological and Planetary Sciences of the California Institute of Technology.

[1] K. Aki and B. Chouet, ''Origin of coda waves: Source, attenuation, and scattering effects,'' J. Geophys. Res. **80**, 3322–3342 (1975).
[2] R. Hennino, N. Trégourès, N. M. Shapiro, L. L. Margerin, M. Campillo, B. A. van Tiggelen, and R. L. Weaver, ''Observation of equipartition of seismic waves,'' Phys. Rev. Lett. **86**(15), 3447–3450 (2001).
[3] R. Benites, P. Roberts, K. Yomogida, and M. Fehler, ''Scattering of elastic waves in 2-D composite media. I. Theory and test,'' Phys. Earth Planet. Inter. **104**, 161–173 (1997).
[4] R. Snieder, A. Grêt, H. Douma, and J. A. Scales, ''Coda wave interferometry for estimating nonlinear behavior in seismic velocity,'' Science **295**, 2253–2255 (2002).
[5] M. L. Cowan, I. P. Jones, J. H. Page, and D. A. Weitz, ''Diffusing acoustic wave spectroscopy,'' Phys. Rev. E **65**, 066605 (2002).
[6] G. Poupinet, W. Ellsworth, and J. Frechet, ''Monitoring velocity variations in the crust using earthquake doublets—An application to the Calaveris fault, California,'' J. Geophys. Res. **89**, 5719–5731 (1984).
[7] M. Campillo and A. Paul, ''Long-range correlations in the diffuse seismic coda,'' Science **299**, 547–549 (2003).
[8] O. I. Lobkis and R. L. Weaver, ''Ultrasonics without a source: Thermal fluctuation correlations at MHz frequencies,'' Phys. Rev. Lett. **87**(13), 134301 (2001).
[9] R. L. Weaver and O. I. Lobkis, ''On the emergence of the Green's function in the correlations of a diffuse field,'' J. Acoust. Soc. Am. **110**, 3011–3017 (2001).
[10] A. Malcolm, J. A. Scales, and B. A. van Tiggelen (submitted).
[11] J. A. Scales and K. van Wijk, ''Multiple scattering attenuation and anisotropy of ultrasonic surface waves,'' Appl. Phys. Lett. **74**, 3899–3901 (1999).
[12] J. A. Scales and K. van Wijk, ''Tunable multiple-scattering system,'' Appl. Phys. Lett. **79**, 2294–2296 (2001).
[13] K. van Wijk, ''Multiple scattering of surface waves,'' Ph.D. thesis, Colorado School of Mines, 2003; K. van Wijk, M. Maney and J. A. Scales, ''1D energy transport in a stongly scattering laboratory model,'' Phys Rev. E (to be published).
[14] D. Komatitsch and J. Tromp, ''Introduction to the spectral-element method for 3-D seismic wave propagation,'' Geophys. J. Int. **139**, 806–822 (1999).
[15] O. Nishizawa, T. Satoh, X. Lei, and Y. Kuwahara, ''Laboratory studies of seismic wave propagation in inhomogeneous media using a laser Doppler vibrometer,'' Bull. Seismol. Soc. Am. **87**(4), 809–823 (1997).
[16] P. Carpena, V. Gasparian, and M. Ortuño, ''Energy spectra and level statistics of Fibonacci and Thue–Morse chains,'' Phys. Rev. B **51**(18), 12813–12816 (1995).
[17] W. Gellermann, M. Kohmoto, B. Sutherland, and P. C. Taylor, ''Localization of light waves in Fibonacci dielectric multilayers,'' Phys. Rev. Lett. **72**, 633 (1994).
[18] L. Dal Negro, C. J. Oton, Z. Gaburro, L. Pavesi, P. Johnson, A. Lagendijk, R. Righini, M. Colocci, and D. S. Wiersma, ''Light transport through the band-edge states of Fibonacci quasicrystals,'' Phys. Rev. Lett. **90**(5), 055501 (2003).
[19] E. Priolo, J. M. Carcione, and G. Seriani, ''Numerical simulations of interface waves by high-order spectral modeling techniques,'' J. Acoust. Soc. Am. **95**, 681–693 (1994).
[20] E. Faccioli, F. Maggio, R. Paolucci, and A. Quarteroni, ''2D and 3D elastic wave propagation by a pseudo-spectral domain decomposition method,'' J. Seismol. **1**, 237–251 (1997).
[21] D. Komatitsch and J. P. Vilotte, ''The spectral-element method: An efficient tool to simulate the seismic response of 2D and 3D geological structures,'' Bull. Seismol. Soc. Am. **88**, 368–392 (1998).
[22] D. Komatitsch and J. Tromp, ''Spectral-element simulations of global seismic wave propagation. I. Validation,'' Geophys. J. Int. **150**, 390–412 (2002).
[23] D. Komatitsch, J. Ritsema, and J. Tromp, ''The spectral-element method, Beowulf computing, and global seismology,'' Science **298**, 1737–1742 (2002).
[24] D. Komatitsch, J. P. Vilotte, R. Vai, J. M. Castillo-Covarrubias, and F. J. Sánchez-Sesma, ''The spectral element method for elastic wave equations—Application to 2-D and 3-D seismic problems,'' Int. J. Numer. Methods Eng. **45**, 1139–1164 (1999).
[25] T. D. Rossing and N. H. Fletcher, *Principles of Vibration and Sound* (Springer, New York, 1995).
[26] H. C. van de Hulst, *Light Scattering by Small Particles* (Wiley, New York, 1957).
[27] A. C. Chang and J. R. Cleary, ''Precursors to PKKP,'' Bull. Seismol. Soc. Am. **68**(4), 1059–1078 (1978).
[28] P. S. Earle and P. M. Shearer, ''Observations of PKKP precursors used to estimate small-scale topography on the core–mantle boundary,'' Science **277**, 667–670 (1997).
[29] A. C. Chang and J. R. Cleary, ''Scattered PKKP: Further evidence for scattering at a rough core–mantle boundary,'' Phys. Earth Planet. Inter. **24**, 15–29 (1981).